Microstructure and Corrosion Behaviour of Carbon Steel and Ferritic and Austenitic Stainless Steels in NaCl Solutions and the Effect of *p*-Nitrophenyl Phosphate Disodium Salt

Mohammed A. Amin[1,2,], Murat Saracoglu[3], N. El-Bagoury[1,4], T. Sharshar[5,6], Mohamed M. Ibrahim[1,7], Joanna Wysocka[8],Stefan Krakowiak[8], Jacek Ryl[8]*

[1] Materials Science and Engineering group, Chemistry Department, Faculty of Science, Taif University, P.O. Box 888, Haweiyah, Saudi Arabia
[2] Chemistry Department, Faculty of Science, Ain Shams University, P.O. Box 11566, Abbassia, Cairo, Egypt
[3] Faculty of Education, Erciyes University, 38039 Kayseri, Turkey
[4] Casting Technology Lab., Manufacturing Technology Dept., Central Metallurgical Research and Development Institute, CMRDI, P. O. Box 87 Helwan, Cairo, Egypt
[5] Physics Department, Faculty of Science, Taif University, P.O. Box 888, Al-Hawiah, Taif 21974, Saudi Arabia
[6] Physics Department, Faculty of Science, Kafrelsheikh University, Kafr El-Sheikh 33516, Egypt
[7] Chemistry Department, Faculty of Science, Kafrelsheikh University, Kafr El-Sheikh 33516, Egypt
[8] Department of Electrochemistry, Corrosion and Materials Engineering, Faculty of Chemistry, Gdańsk University of Technology, Narutowicza Str. 11/12, 80-233 Gdańsk, Poland
[*]E-mail: maaismail@yahoo.com

The microstructure and corrosion behavior of carbon steel (CSA516) and ferritic (SS410) and austenitic (SS304L) stainless steels were studied and compared. Corrosion tests were carried out in 0.5 M NaCl solutions. Rates of corrosion were monitored based on weight loss, Tafel extrapolation and linear polarization resistance (LPR) methods. Rates of corrosion were ranked following the order: CSA516 >> SS410 > SS304L. The impact of *p*-Nitrophenyl phosphate disodium salt (NPP) on the corrosion rate of CSA516 was also studied using Tafel polarization and LPR measurements. Optical microscopy (OM), scanning electron microscopy (SEM/EDX), and X-ray photoelectron spectroscopy (XPS) were employed to assess the chemical compositions and morphologies of the corroded and inhibited surfaces. FT-IR analyses were also performed to assess the functional groups of the inhibited sample in a comparison with NPP itself. XPS and FT-IR studies revealed the presence of phosphate groups originating from tested inhibitor, thus proving formation of the protective layer on the steel surface. The microstructural and defect investigations of as-polished, corroded, and inhibited CSA516 samples were also carried out using positron annihilation lifetime (PAL) and positron annihilation Doppler broadening (PADB) techniques. Experimental findings revealed that NPP acted as an efficient

mixed-type inhibitor with anodic predominance. It reached about 97% inhibition efficiency at a low concentration of 0.02M.

1. INTRODUCTION

Steel materials have found wide applications in a broad spectrum of industries and machinery; despite their tendency to corrosion. For these reasons, most of the corrosion research groups around the world devoted themselves to effectively control steel corrosion in various aggressive media employing different methods [1-4]. A particularly high inhibitor efficiency on steel is usually achieved with anodic inhibitors, that consists of oxidizing agents, i.e. substances with the ability to accept electrons in electrochemical redox reactions. An anodic inhibitor oxidizes Fe^{2+} ions to ferric ions, leading to the formation of a dense oxide film on the surface of the steel, and a subsequent suppression of the anodic part of the corrosion reaction. The precipitated ferric product blocks the transport of ferrous ions into the electrolyte [5]. Corrosion inhibition mechanism of anodic inhibitors is based on their reaction with corrosion products, forming a cohesive and insoluble film on metal surface [6]. Effective corrosion inhibition requires the use of inhibitor concentration that is sufficient for the film to fully cover surface area. Otherwise the corrosion rate of metal may even increase and localized pitting corrosion may occur. The use of mixtures of two or more compounds as corrosion inhibitors often provides higher corrosion inhibitor efficiency, additionally minimizing costs of metal protection [7-10]. The synergistic effects have been ascribed to different alloys, such as stainless steels [11], copper [12] mild steel [13] and light metal alloys [14,15]. The mechanism behind synergism is also explained in different ways; for instance in the case of Al-Cu alloys it is said that 8-8-hydroxyquinoline interacts with alloys matrix while BTA effect is limited to the copper-rich intermetallic particles [14].

However, most of highly efficient inhibitors are organic compounds which are toxic and carcinogenic. Such harmful effects motivated the researchers to search eco-friendly and harmless materials as efficient anticorrosion agents [16-22]. The objective of a part of our research is to apply safe inorganic and organic compounds as effective corrosion inhibitors for some metals and alloys in a variety of corrosive environments [23–32]. *p*-Nitrophenyl phosphate disodium salt (NPP) is a chromogenic substrate for the determination of acid and alkaline phosphatase enzymes and also used for diagnostic manufactures and clinical laboratories [33-35]. It undergoes hydrolysis in aqueous electrolytes, with the formation of p-nitrophenolate and disodium hydrogen phosphate. These compounds are often ascribed as anodic corrosion inhibitors therefore offering a natural potential of synergistic interaction. To the best of our knowledge, there are no reports in the literature concerning the application of NPP as a corrosion inhibitor. Therefore, the objective of this work is to gain some insight into the effect of NPP as a safe-inhibitor for mild steel corrosion in a NaCl solution. Measurements were conducted in 0.5 M NaCl solutions as a function of NPP concentration employing chemical (weight loss) and electrochemical (Tafel polarization and LPR) techniques, complemented by

ex situ OM, SEM/EDX, FT-IR, and XPS examinations of the corroded and inhibited surfaces. The inhibition mechanism induced by NPP is discussed based on XPS studies. The electron density and corrosion-related defects in corroded and inhibited steel samples were also assessed using PAL and PADB techniques. Such techniques were applied to probe the small changes of microstructure and defects in different types of materials, including steel samples [36-42], and also used to investigate corrosion of some metals and alloys [23, 43-48]. The thermalized and diffused positron in solids annihilates as free particle or forms a positronium atom (Ps). For positron annihilation lifetime (PAL) technique, the measured lifetimes (τ_i) and their intensities (I_i) of the positrons in metals depend on their microstructure and defect distribution at the annihilation site. In positron annihilation Doppler broadening (PADB) technique, the line–shape of annihilation γ ray, S (for shape), and W (for wings), gives the momentum distributions of electrons at the annihilation site.
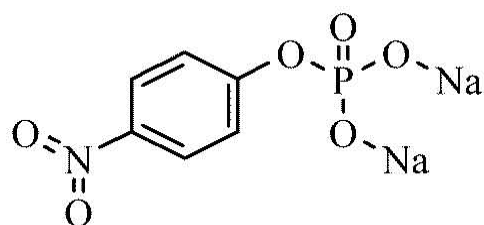
2. EXPERIMENTAL

2.1. Materials and Solutions

Table 1. Chemical composition of the three tested steel materials.

Alloy	Alloying elements (%)					
	C	Si	Mn	Cr	Ni	Fe
CSA516-70	0.18	0.13	0.18	0.00	0.00	bal.
SS410	0.15	0.48	0.35	12.59	0.50	bal.
SS304L	0.03	0.46	0.73	18.43	7.91	bal.

The tested samples employed in this work are carbon steel (A516-70) and stainless steels (SS410 and SS304L) of chemical composition shown in Table 1. These materials were in the form of cylinder coupons, outer and inner diameter 1.250 and 0.375 inch, respectively and thickness 0.125 inch. All chemicals used in the present work, including the organic compound that is tested as an inhibitor, were purchased form Aldrich and used as received. The chemical structure of NPP is given below:

4-Nitrophenyl phosphate disodium salt (NPP)

2.2. Methods

2.2.1. Weight loss measurements

Prior to each experiment, the tested samples were first grounded using 1200# grit SiC paper and then ultrasonically cleaned in ethanol. For data repeatability, two samples were used in each weight loss test. Corrosion rates were calculated on the base of mass changes of the samples, these measurements were conducted on an analytical electron balance (0.0001 g in accuracy), according with ASTM G1 procedure [49]. The corrosion behavior of coupon specimens was evaluated by measuring the mass loss as a function of the immersion time (after 1, 3, 7, 14 and 30 days). After completion of exposition corrosion products were removed adopting a cleaning procedure based on ASTM G1 [49]. The cleaning procedure was repeated on samples 7-10 times to reach a steady state, with mass loss determined after each cleaning. Finally, the mass loss was graphed as a function of the number of cleaning cycles to get the mass of the corrosion products. The composition of the bath used in the cleaning procedure is: 0.5 L HCl (sp gr 1.19) + 3.5 g hexamethylene tetramine + 1L H_2O [49].

2.2.2. Microstructure studies

After final scratch free polishing and cleaning using ultrasonic cleaner, the following etchant baths were used prior to investigating the microstructure of carbon steel and SS304L samples: (i) the etchant bath for the carbon steel sample was 2% nital (2 ml HNO_3 and 98 ml Ethyl), and (ii) that for the SS304Lwas a solution of 500 ml distilled water, 300 ml hydrochloric acid , 200 ml nitric acid, 50 ml of a saturated iron-III-chloride solution, 2.5 g copper-II-chloride.

2.2.3. Electrochemical measurements

Electrochemical measurements and surface analysis was carried out on sheets, cut out from each coupon. Sheet dimensions were (0.7 cm) × (1.5 cm) × (0.25 cm; thickness). Prior to measurements, all sides of each sheet but one were isolated to obtain an analysis surface of 0.175 cm^2 (0.70 x 0.25) and afterwards immersed in the test solution.

Linear polarization resistance (LPR) and Tafel plots were employed to monitor the corrosion rates of investigated steel samples and to assess corrosion inhibition efficiency of NPP. These studies were performed using Autolab PGSTAT30 (potentiostat/galvanostat/FRA) from Ecochemie (The Netherlands), connected to a personal computer. The measurements were carried out in three-electrode setup, with investigated sample as working electrode, saturated calomel electrode (SCE) in Luggin-Haber capillary as reference electrode and platinum spiral as counter electrode. Electrochemical cell volume was 100 mL. The measurements were carried out in naturally aerated uninhibited and inhibited solutions at 25 °C ±1 °C, controlled with the use of a water thermostat.

Prior to electrochemical study, open circuit potential (OCP) was measured for the period of 24 h. Afterwards, the linear polarization resistance (LPR) was used to study the corrosion inhibition behavior and the polarization resistance, R_p, of thin film of inhibitor that formed on the electrode surface. The LPR curves were recorded in the potential range of -20 to +20 mV with respect to OCP at

a scan rate of 0.2 mV s^{-1}. Finally, Tafel polarization plots were used to determine the corrosion potential (E_{corr}) and corrosion current density (j_{corr}) of the corroded and inhibited surfaces. The potentiodynamic polarization curves were recorded in a potential window of -0.25 to +0.25 V with respect to OCP at a scan rate of 1.0 mV s^{-1}.

2.3. Surface analysis

Metallurgical miscoscope (MX7520, Camera Infinity 1, MEIJI TECHNO, Japan) and scanning electron microscope (JEOL JSM 6390 LA) served to examine morphology of corroded and inhibited metal surfaces. Composition of each sample was determined by means of energy-disperstive X-ray spectroscopy (EDS) obtained by EDS attachment on JEOL SEM (JEOL EDS EX-54175JMU) and ZAF software. FT-IR analysis was carried out to determine the functional groups on the surface of the inhibited sample in a comparison with the inhibitor itself. The FT-IR spectra were recorded using Alpha-Atunated FT-IR Spectrophotometer, Brunker in the range of 400-4000 cm^{-1}. Detailed analysis of surface chemical composition was performed on the basis of X-Ray Photoelectron Spectroscopy (XPS) with Escalab 250Xi (ThermoFisher Scientific, United Kingdom) equipped in monochromatic Al X-Ray source. High resolution spectra were made at a pass energy of 10 eV, and energy step size of 0.1 eV. X-ray spot size was 650 µm. XPS measurements were normalized by calibration of the X axis (binding energy) for neutral carbon C1s peak (at 284.6 eV).

2.4. PAS measurements

2.4.1. PAL measurements

A fast-fast coincidence spectrometer was used to carry out the PAL measurements [50]. The time resolution (FWHM) of this spectrometer, measured with ^{60}Co source at ^{22}Na energy window settings, was ~310 ps. Two Bicron BC-418 plastic scintillation detectors were used to detect the γ rays and the signals from both detectors were processed using Ortec modules. A 10 µCi ^{22}Na source and two identical sheets of as-polished, corroded or inhibited CSA516 samples were arranged in the 4π configuration [50]. The PAL measurements were performed in air at room temperature. The accumulated count for each lifetime spectrum was more than one million counts. Each sample was measured three times. The time interval between the 1274.5 keV γ ray emitted by the ^{22}Na radioisotope and one of the annihilation radiations was used to measure the positron annihilation lifetime. A computer program LT was used to analysis the resulting lifetime spectra [51]. The lifetime spectra of the CSA516 samples were decomposed into two components τ_1 and τ_2 with the associated formation probabilities I_1, and I_2. The τ_1 describes positron annihilation in a single vacancy on edge dislocation in iron [40] and in vacancy-solute complexes for steel components [52]. The τ_2 represents ortho-Ps formation in microcracks caused by the agglomeration of more than 30 vacancies [40]. The best-fitting parameter of all exponential components of the measured lifetime spectra ranged from 1.1 to 1.4. The range of the experimental errors for the PAL parameters τ_1, τ_2, I_1 and I_2, determined over multiple measurements, were found to be < 1.4 ps, < 500 ps, 0.02**%** and 0.03**%**, respectively. The average

radius of the microcracks, *R*, is determined using a semiempirical equation with the values of τ_2 [53,54].

2.4.2. PADB measurements

The PADB measurements were carried out under the same experimental configuration as for PAL measurements. A 25% p–type HPGe detector (Ortec, GEM series) was used to measure the DB line–shape parameters (*S* and *W*) in air at room temperature. The energy resolution (FWHM) of the HPGe detector was 1.6 keV for 1.33 MeV γ line of [60]Co. An Ortec 919 multichannel analyzer (MCA) was used to acquire the amplified signals from an Ortec 570 amplifier. The energy calibration of the gamma-ray spectrometer (68 eV/channel) was measured using the [133]Ba source. For each spectrum, the net count under the annihilation line was more than two million counts. The *S*–parameter is defined as the ratio of the integration over the central part of the annihilation line to the total integration [55]. The annihilation with high momentum core electrons can be measured using the *W*–parameter that is defined as the ratio of counts in the wing regions of the peak to the total counts in the peak. The equation used to calculate the *S*– and *W*–parameters were reported [56]. The SP ver. 1.0 program was used to analysis the DB spectra [57]. The centroid channel with maximum counts of the 511 keV peak was carefully defined as it is the base for calculations of *S*– and *W*–parameters. The input data for this program are fixed for all spectra of the studied samples.

3. RESULTS AND DISCUSSION

3.1. Monitoring rates of corrosion

3.1.1. Mass loss measurements

The plots of the loss in mass (Δ*m*) of the products of the corrosion process versus number of the cleaning cycles were constructed for the three tested samples after 1, 3, 7, 14, and 30 days of immersion in 0.5 M NaCl solutions at 25 ºC. Figures 1a-d are representative examples for the data obtained after 3, 7, 14 and 30 days of immersion, respectively. In all cases, two intersecting straight lines, namely BC and AB were obtained. Obviously, the line AB is more steeper than BC, characteristic for the formation of a surface film (corrosion products) due to corrosion [49]. Literature revealed that the presence of the corrosion products as a surface film, the abundance of which on the corroded surface depends on its solubility, can alter the kinetics of mass loss [28,30,58-69]. Soluble corrosion products, i.e., no surface film, yielded Δ*m vs.* time linear plots [30,58,59]. In other cases, soluble corrosion products led to Δ*m vs.* time plots with typical straight lines go through the origin, thus fitting zero order kinetics [28,59-69]:

$$\Delta m \ (\text{or uniform corrosion rate}) = k\,t \tag{1}$$

where *k* (can be considered as a measure for the uniform corrosion rate) is the rate constant of the zero order reaction and *t* is the immersion time [59].
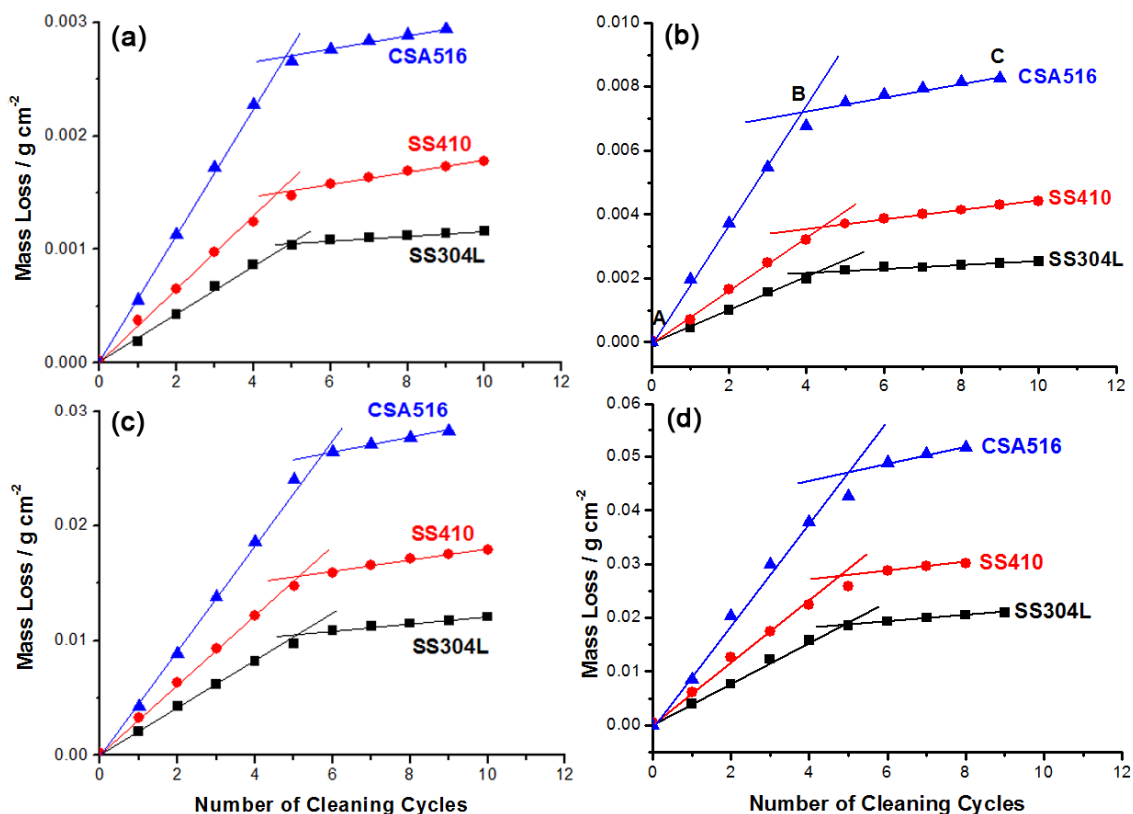
Figure 1. Mass loss *vs.* number of cleaning cycles recorded for the three tested samples in 0.5 M NaCl at 25 °C after **(a)** 3, **(b)** 7, **(c)** 14 and **(b)** 30 days of immersion.

On the other hand, incomplete removal of corrosion products due to solubility issues caused the plots of Δm - t deviate from linearity. The case that is highly common and well documented in the literature, see for example *Refs.* [24,31,70,71].

Based on the above arguments, corrosion products on the surface should be controlled during mass loss measurements. According to ASTM [72], to avoid corrosion products' accumulation, the test solution to test specimen minimum ratio should be at least 15 mL cm^{-2}. Here, this ratio is about 50 mL cm^{-2}. Referring again to Fig. 1, corrosion products start to dissolve leaving the surface from point A. This process of corrosion products' removal continue till point B, where they are assumed to be completely removed. The straight line following AB, namely BC therefore represents corrosion of the bare alloy surface. This means that the mass loss at point B is due to the corrosion products, and can be considered here as a correction factor (m_{cf}) for mass loss measurements, based on Eq. (2) [49]:

Actual mass loss (Δm) = $m_i - (m_f + m_{cf})$ (2)

Where m_i is the initial mass (mass of the sample before the corrosion test), m_f is the final mass (mass of the sample after the corrosion test; the sample is simply dried, but not chemically treated for the corrosion products, i.e., no cleaning process), and m_{cf} is the mass of the corrosion products (evaluated from Fig. 1). The mass loss data were used to calculate the average corrosion rates, in mpy (Mils per year), for the three tested samples in the test solution (0.5 M NaCl) using Eq. 3 [49].

Corrosion Rate (mpy) = $(K \times \Delta m)/(A \times T \times D)$ (3)

where K is a corrosion constant [49], Δm is the mass loss in grams, D is the metal density in g cm^{-3}, A is the area of sample in cm^2, and T is the time of exposure of the metal sample in hours. Figure 2 display average rates of corrosion *vs* time.
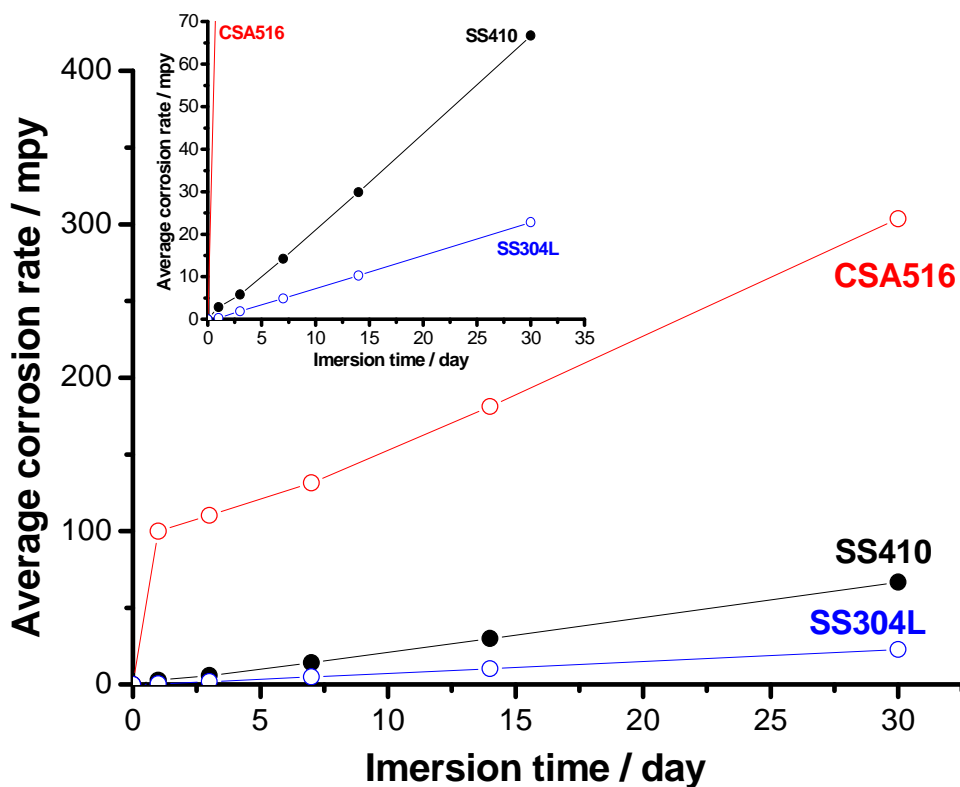

Figure 2. Average corrosion rates *vs.* immersion time (1-30 days) plots of the three tested samples in 0.5 M NaCl at 25 ^{o}C.

It is seen from Fig. 2 that, at any given immersion time, the corrosion rate of the studied samples decreases according to the sequence: CSA516 >> SS410 > SS304L. The average rates of corrosion recorded for the two tested stainless steels, namely SS410 and SS304L obey the rate law of zero order reaction over the entire immersion period, Eq. 1, inspect the inset of Fig. 2. On the contrary, the average corrosion rates of the carbon steel sample (CSA516) deviate significantly from the zero order kinetics, most probably due to corrosion products' accumulation [49]. The zero order kinetics of the two tested stainless steels, particularly SS304L, is expected as their surfaces are almost free from corrosion products (highly corrosion resistant), even after 30 days of immersion in the corrosion test solution. Similar findings were previously obtained in our laboratory [59].

3.1.2. Polarization measurements

Rates of corrosion were also monitored electrochemically employing Tafel extrapolation, Fig. 3(a), and LPR, Fig. 3(b), methods. The various electrochemical corrosion parameters derived from such polarization measurements are presented in Table 2.

Table 2. Mean value (standard deviation) of the various electrochemical parameters, together with the rates of corrosion, obtained from Tafel extrapolation and linear polarization resistance methods performed for the three tested alloys 0.5 M NaCl solutions at 25 °C.

Tested alloy	Tafel extrapolation method					LPR method		
	$-E_{corr}$ / mV(SCE)	$-\beta_c$ / mV dec^{-1}	β_a / mV dec^{-1}	j_{corr} / μA cm^{-2}	CR / mpy	R_p / kΩ cm^2	j_{corr} / μA cm^{-2}	CR / mpy
CSA516	761(10)	342(3.1)	200(2.2)	209(3.2)	97.9(1.4)	0.28(0.03)	199(2.6)	93(1.2)
SS410	483(7)	176(2.2)	207(2.8)	6.3(0.11)	2.71(0.06)	15.95(0.2)	6.02(0.08)	2.6(0.04)
SS304L	326(5)	160(1.6)	598(5.7)	0.6(0.07)	0.24(0.03)	274(2.8)	0.50(0.06)	0.2(0.03)

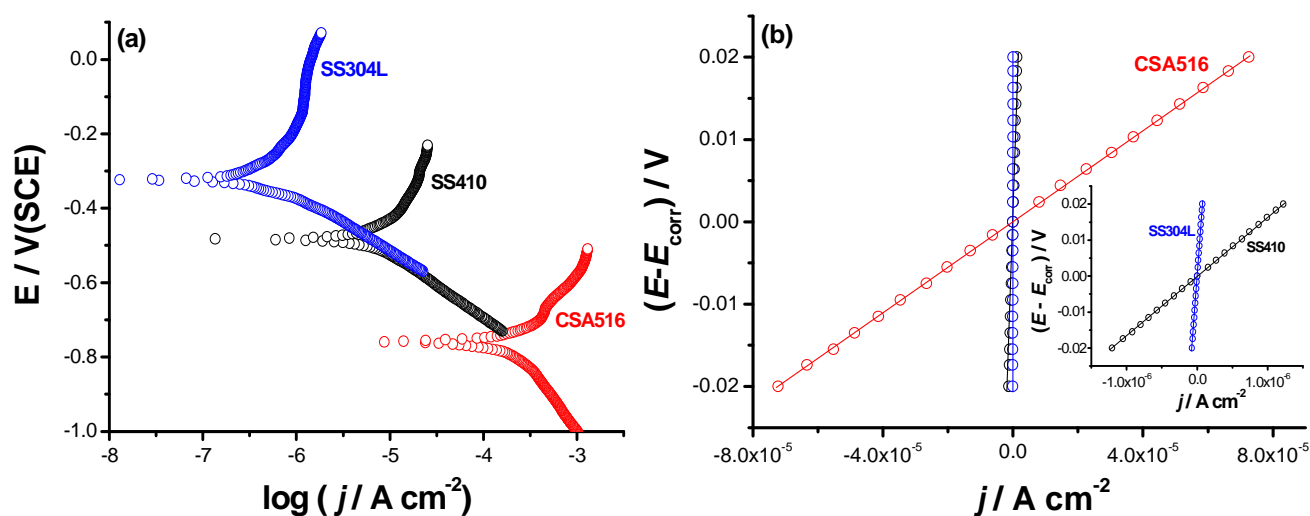**Figure 3.** **(a)** Cathodic and anodic polarization curves and **(b)** plots of linear polarization resistance (LPR) measurements recorded for the three tested alloys in 0.5 M NaCl solutions at a scan rate of 0.2 mV s^{-1} at 25 °C.

Close inspection of Fig. 3(a) reveals that the cathodic branches of the polarization curves exhibit a typical Tafel behavior, which helps determine the cathodic Tafel slope (β_c) and corrosion currents (j_{corr}) by the Tafel extrapolation method accurately. On the other hand, the Tafel behavior does not exist in the anodic domains; instead a curvature (most probably caused by the anodic passivation processes) results covering all the applied potential range. This curvature makes evaluation of the anodic Tafel slopes (β_a) inaccurate [73-75]. This was the reason why the values of j_{corr} and β_a evaluated by the software not included here. To overcome this problem, and to get more accurate values for β_a (and hence for j_{corr}), mathematical treatments based on the work of McCafferty [76] were performed on the experimental anodic branches to generate the calculated anodic Tafel lines.

It follows from Fig. 3(a) that CSA516 exhibited the lowest anodic and cathodic overpotentials (and hence the highest rates of corrosion) among the tested alloys. This is obvious from the data of Table 2, which showed that CSA516 recorded a j_{corr} value of 209 μA cm^{-2}, employing Tafel

extrapolation method, which is 33 times greater than that recorded for SS410 (6.3 µA cm^{-2}) and 348 times greater than that measured for SS304L (0.6 µA cm^{-2}). These findings demonstrate the extremely low corrosion resistance of CSA516 as compared with SS410 and SS304L, thus supporting weight loss measurements.

The values of j_{corr} (measured in µA cm^{-2}) calculated from Tafel extrapolation and LPR measurements (Table 2) can be related directly to the corrosion rate through the following equation [77].

$$\text{Corrosion rate (mpy)} = \{0.13\, j_{corr}\, (E.W.)\}/D \tag{4}$$

where $E.W.$ is the equivalent weight of the corroding species, in g, and D is the density of the corroding species, in g cm^{-2}. Corrosion rates obtained from Tafel extrapolation and LPR methods are also presented in Table 2. An agreement can be seen in the corrosion rate values measured from the two methods. Values of the anodic and cathodic Tafel slopes (β_a and β_c) obtained from the analysis of the Tafel plots (Fig. S1 and Table 2) and those of the polarization resistance, $R_p = (dE/dj)_{E=E_{corr}}$, obtained from the slopes of the LPR plots, Fig. 3(b), are introduced in Stern-Geary equation [78] to get accurate values for j_{corr}, Table 2.

$$j_{corr} = B/R_p = \{\beta_a\, \beta_c\, /2.303(\beta_a + \beta_c)\}\, /\, R_p \tag{5}$$

A good agreement can be observed between the values of j_{corr} evaluated from the two polarization methods. As clearly seen in Table 2, SS304L recorded the largest R_p value (274 kΩ cm^2), i.e., the highest corrosion resistant alloy, among the tested alloys, which is ~ 10^3 times greater than that measured for CSA516 (0.28 kΩ cm^2) and 17 times greater than that recorded for SS410 (15.95 kΩ cm^2). Thus LPR and Tafel extrapolation methods go parallel with each other and support weight loss measurements revealing the extremely high corrosion resistance of SS304L as compared with SS410 and CSA516.

3.1.3. Microstructure studies

The microstructure of the carbon steel CSA516 can be used to account for its low corrosion resistance as compared with SS410 and SS304L. The morphologies of as-polished surfaces of CSA516 and SS304L as a reference point, are shown on Fig. 4a-b. Both surfaces have some scratches due to the polishing process as well as some black points especially on the surface of stainless steel specimen, (Fig. 4b). These black points could be either carbides or cavities. The microstructure of the carbon steel CSA516 and SS304L is shown in Fig. 4c-d. In addition to iron carbides, the microstructure of CSA516, shown on Fig. 4c, consists of pearlite (ferrite + cementite, Fe$_3$C) as a matrix phase in addition to the ferrite phase. However, the microstructure of the stainless steel alloy, Fig. 4d, contains ferrite phase, parent phase, and austenite phase found in interdendritic zones. Additionally, there are some sulfides in the microstructure of this alloy. The analysis of these inclusions is presented in Table 3. The multiphase structure, namely pearlite (ferrite + cementite, Fe$_3$C) as a matrix phase in addition to the ferrite phase, in the microstructure of CSA516 is the main reason behind its very low corrosion resistance. The presence of both ferrite and pearlite grains in the microstructure create galvanic cells, thus corrosion is accelerated [59].
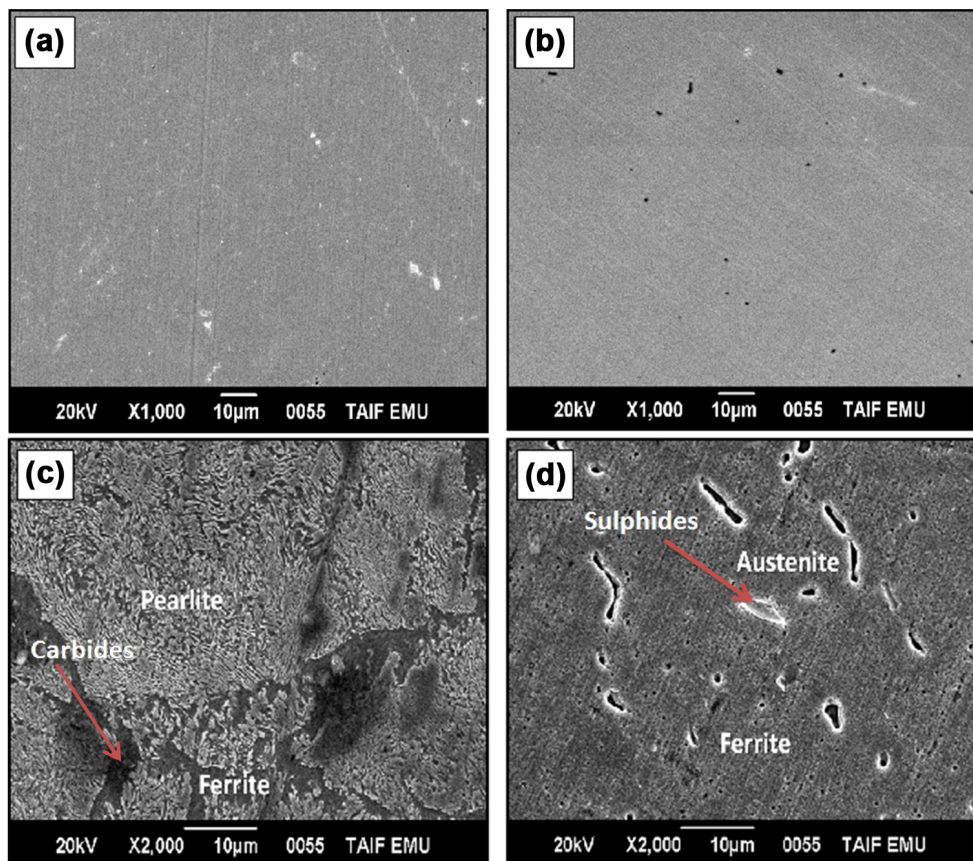
Figure 4. SEM images of as-polished **(a)** CSA516 and **(b)** SS304L surfaces, and their morphology change after etching (see the experimental part, section 2.2.2) for **(c)** CSA516 and **(d)** SS304L.

Another galvanic cells may also exist in the carbon steel's microstructure participating in accelerating corrosion further. These may form due to pearlite, which is a mechanical mixture of lamellar ferrite and lamellar iron carbide (cementite), components. On the other hand, the high corrosion resistance of the two studied ferritic and austenitic stainless steels is mainly attributed to their Cr content, in SS410 (> 12%) and in SS304L (> 18%). Cr in such stainless steel alloys reacts with the atmospheric oxygen to form a highly protective thin, invisible layer of Cr-oxide passive film.

Table 3. Chemical analysis of carbides and sulfides exist in the microstructure of CSA516 and SS304L (in wt.%).

Chemical analysis	C	S	Mn	Cr	Ni	Mo	Fe
Carbides	7.57	--	--	--	--	--	92.43
Sulfides	--	6.52	7.06	25.53	3.53	10.97	46.40

This Cr-oxide passive film is highly protective in case of SS304L than in SS410, due to the high Cr content included in the matrix of the former alloy [79]. In addition, SS410 may also form carbides (Fe and Cr carbides), which greatly diminish its corrosion resistance against SS304L, due to its high C content. Another important reason for the extremely high corrosion resistance of SS304L as compared with SS410 is the high Ni content (~8.0%) of the former. The high Ni in SS304L is expected

to stabilize the austenite phase in the microstructure of SS304L. This in turn results in a single phase structure with very high corrosion resistance; no galvanic cells are expected to form [80]. This trend is expected to be ineffective in SS410 due to its low Ni content (< 1.0%).

3.2. Corrosion inhibition studies of carbon steel (CSA516) using NPP

3.2.1. Tafel polarization and LPR measurements

The above findings, based on chemical and electrochemical measurements, chemical composition and microstructure points of view, demonstrated that the corrosion resistance of CSA516 is the worst among the tested alloys. The objective of this section is to enhance the low corrosion resistance of CSA516 via adding an inhibitor (NPP) to the corrosive medium. Measurements were conducted in 0.5 M NaCl solutions without and with various concentrations of NPP (C_{NPP}: 0.001 – 0.02 M) at a scan rate of 0.2 mV s^{-1}, employing Tafel polarization (Fig. 5(a)) and LPR (Fig. 5(b)) measurements. Fig. 5(a) reveals that the cathodic and anodic branches of the polarization curves are shifted toward lower currents, accompanied with a marked anodic shift in E_{corr}, with increase in C_{NPP}. These results indicate the inhibiting influence of NPP on the NaCl corrosion of steel. It is obvious that the anodic curves are markedly affected by the inhibitor than the cathodic ones, meaning that the additive inhibits steel corrosion by controlling mainly the anodic reaction (an anodic-type inhibitor). This occurs by blocking the anodic sites on the steel surface via adsorption. The inhibitor adsorption on the anodic sites is expect for the first sight to take place through the lone pair of electrons of its hetero-atoms (namely N, O, and P), multiple bonds and the π-cloud of the aromatic ring. More details regarding the inhibition mechanism are presented in section 3.2.2., based on SEM/EDX, FT-IR, and XPS examinations.
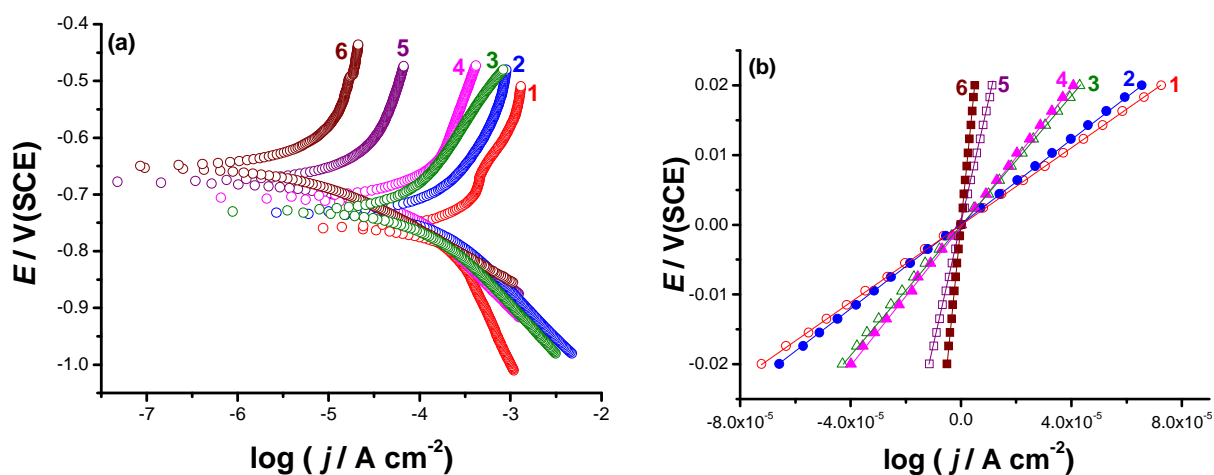

Figure 5. (a) Cathodic and anodic polarization curves and **(b)** plots of linear polarization resistance (LPR) measurements recorded for CSA516 in 0.5 M NaCl solutions without and with various concentration (0.001-0.02 M) of NPP at a scan rate of 0.2 mV s^{-1} at 25 °C. Blank; (2) 0.001 M NPP; (3) 0.002 M NPP; (4) 0.005 M NPP; (5) 0.01 M NPP; (6) 0.02 M NPP.

The various electrochemical kinetic parameters associated with Tafel polarization measurements were evaluated adopting McCafferty's mathematical treatments [76] for each polarization curve in Fig. 5(a), revisit Figure S3. The parameters obtained from the analysis of the Tafel extrapolation method, together with those extracted from the LPR method based on the slopes of the lines in Fig. 5(b) and equation 5, are presented in Table 4.

The values of j_{corr} presented in Table 4 were introduced in equations 4 and 6 to respectively calculate the rate of corrosion and inhibition efficiency (ε) values as a function of C_{NPP}, Table 4.

$$\varepsilon\ (\%) = \{(j_{corr})_o - (j_{corr})_i\}\ /\ (j_{corr})_o \tag{6}$$

where $(j_{corr})_o$ and $(j_{corr})_i$ are the corrosion current densities for uninhibited and inhibited NaCl solutions, respectively. A good agreement between the two polarization methods can be observed. It follows from Table 4 that the values of j_{corr} decrease, while those of R_p increase, with C_{NPP}, corresponding to improved inhibition performance. For instance, adopting Tafel extrapolation method, the value of ε has increased from 31.2% at $C_{NPP} = 10^{-3}$ M to 96.8% at $C_{NPP} = 0.02$ M.

Table 4. Mean value (standard deviation) of the various electrochemical parameters, together with corrosion rate and inhibition efficiency values, obtained from Tafel extrapolation and linear polarization resistance methods performed for CSA516 electrode in 0.5 M NaCl solutions without and with various concentration (0.001 – 0.02 M) of NPP at 25 ^{o}C.

$C_{inhibitor}$ / M	$-E_{corr}$ / mV(SCE)	Tafel extrapolation method $-\beta_c$ / mV dec^{-1}	β_a / mV dec^{-1}	j_{corr} / μA cm^{-2}	CR / mpy	ε (%)	LPR method R_p / kΩ cm^2	j_{corr} / μA cm^{-2}	CR / mpy	ε (%)
Blank	761(10)	342(3.1)	200(2.2)	209(3.2)	97.9(1.4)	-----	0.28(0.03)	199(2.6)	93(1.2)	-----
0.001	731(8)	158(1.6)	236(2.4)	144(1.7)	67.4(1.1)	31.2(0.8)	0.3(0.033)	139(1.6)	65.1(0.9)	30(0.7)
0.002	729(9)	170(1.8)	290(2.6)	109(1.4)	51(0.88)	47.9(1.05)	0.46(0.042)	101(1.3)	47.3(0.7)	49.1(0.95)
0.005	706(7)	160(1.6)	142(1.7)	60.3(1.2)	28.2(0.6)	71.2(1.1)	0.52(0.053)	62.4(1.1)	29.2(0.5)	68.6(1.03)
0.01	677(6)	120(1.3)	480(4.5)	25(0.8)	11.7(0.32)	88.1(1.18)	1.75(0.062)	23.8(0.9)	11.2(0.3)	87.9(1.1)
0.02	651(6)	90(1.1)	270(2.8)	6.7(0.3)	3.1(0.07)	96.8(1.3)	4.07(0.08)	7.2(0.4)	3.4(0.06)	96.3(1.16)

3.2.2. Surface analysis

Figure 6 shows OM images for the corroded and inhibited surfaces of the carbon steel after 24 h of immersion in 0.5 M NaCl solution at 25 ^{o}C. Obviously, the corrosion of steel is significantly suppressed upon introducing NPP to the corrosive medium, where the corroded areas (image a) were significantly decreased and almost disappeared in the presence of NPP, image b. This was also quite clear from visual observations, which revealed that the surface of the corroded sample was covered with the corrosion products, as shown in the inset of Fig. 6a. On the contrary, the inhibited sample (inset of Fig. 6b) was almost free from the corrosion products. SEM examinations came to the same conclusion, as shown in Fig. 7.

The inhibiting effect of the NPP molecules may be attributed to their adsorption and subsequent formation of a protective film on the electrode surface, as evidenced from EDX analysis. Such analysis revealed that in inhibitor-free solution, the corroded steel surface is mainly Fe (93.30 mass %), located at a binding energy of 6.398 keV/Kα. Contributions from some alloying elements,

namely C (0.277 keV/Kα, 0.16 mass %), Si (1.739 keV/Kα, 0.15 mass %), and Mn (5.894 keV/Kα, 0.13 mass %) were also detected.
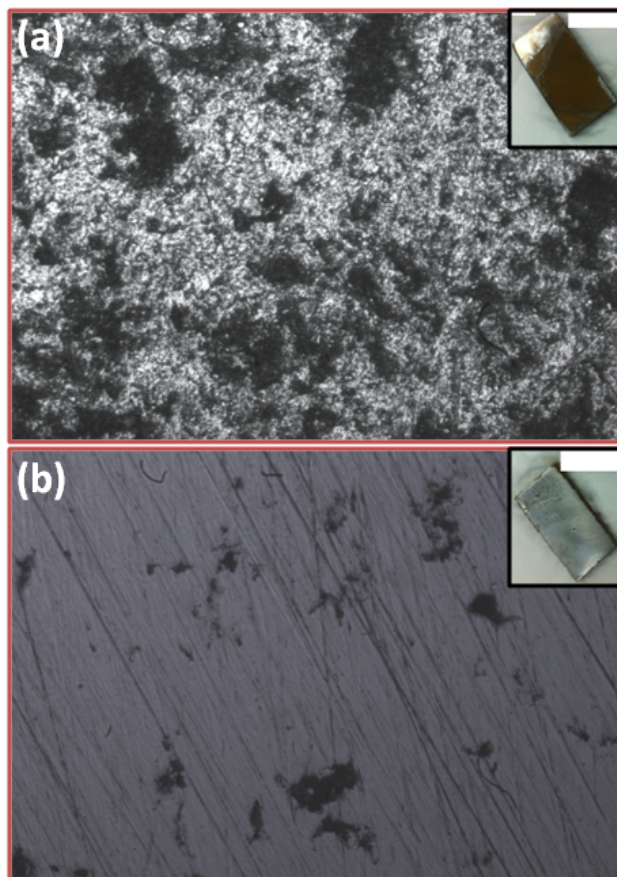

Figure 6. Optical microscope images for (a) corroded and (b) inhibited CSA516 samples obtained after 24 h of immersion in NaCl solutions without (corroded) and with 0.01 M NPP (inhibited) at 25 ºC. Insets are the visual observations of the corroded and inhibited samples.

A signal for O (0.525 keV/Kα, with a mass percent of 5.22) was observed, most probably due to some corrosion products (oxides and/or hydroxides) strongly adhered to the surface. Also, a detectable amount of adsorbed Cl (2.621 keV/Kα, with a mass percent of 1.04) was recorded. The low contribution from O may be due to destabilization (oxide thinning/dissolution) of the passive film on steel promoted by adsorbed Cl⁻ anions. On the other hand, in the presence of the inhibitor (NPP), the EDX spectra showed an additional signal for P (2.013 keV/Kα, with mass percents of 1.28) due to the phosphate group of NPP. The N signal due to the p-nitro group of NPP did not appear and there is no additional contribution for the C signal. At the same time, the contribution of the O signal is enhanced, most probably because of the oxygen atoms of the adsorbed NPP molecules. The absence of N and C from the inhibited surface may indicate that the aromatic part of NPP, namely the nitrophenyl group did not adsorb and went to the solution as a soluble species.
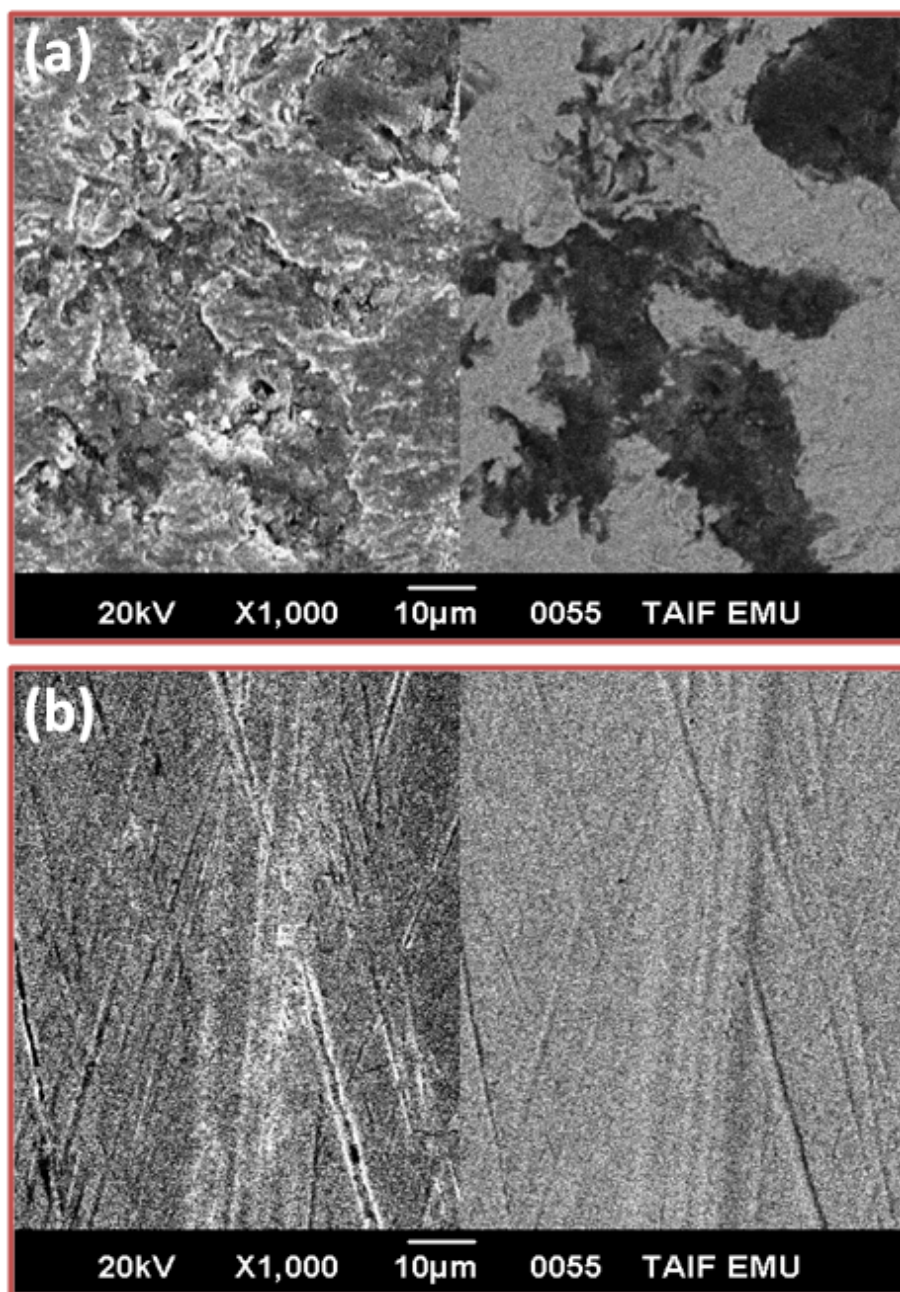
Figure 7. SEM images for (a) corroded and (b) inhibited CSA516 samples obtained after 24 h of immersion in NaCl solutions without (corroded) and with 0.01 M NPP (inhibited) at 25 °C.

To confirm this, FT-IR analysis of the inhibited sample was performed and compared with NPP itself, Fig. 8. The results revealed the adsorption of the phosphate group, where the IR absorption bands related to the inhibitor itself (NPP) have been disappeared for the inhibited sample, and new absorption bands at 2362 and 1365 cm^{-1} have been observed.

These bands are assigned to the stretching vibration of $v_{st}(O=)PO-H$ and $v_{st}(P=O)$, respectively [81]. Based on EDX and FT-IR analyses, it can be proposed here that a carbonaceous material containing O and P atoms has covered the surface, protecting it against corrosion.
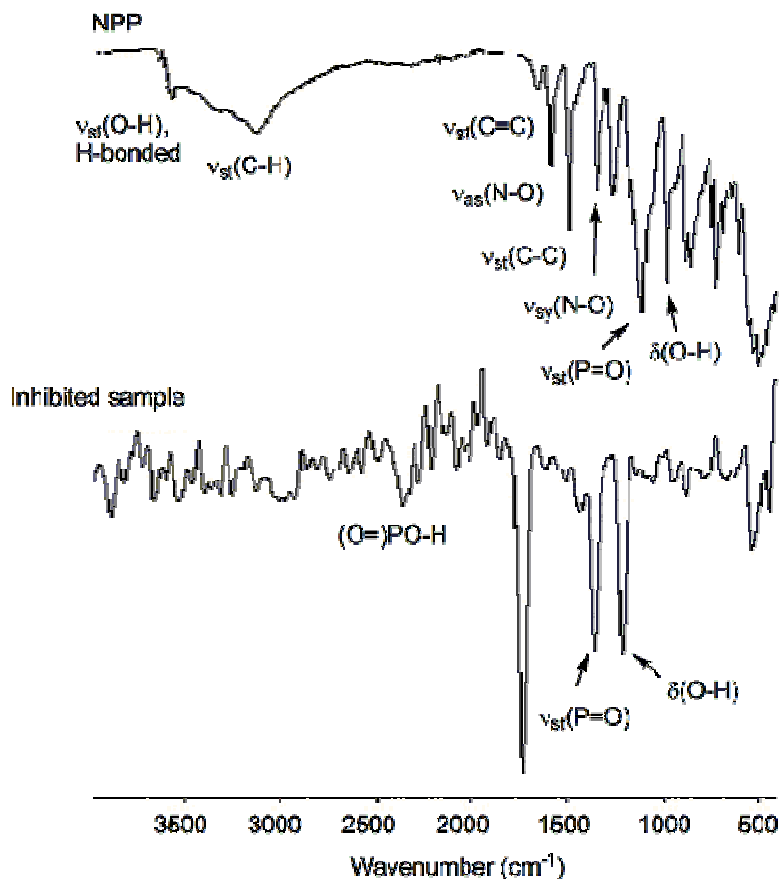
Figure 8. FT-IR spectra recorded for the inhibitor molecule (NPP) itself and the inhibited CSA516 sample obtained after 24 h of immersion in (0.5 M NaCl + 0.01 M NPP) solution at 25 °C.
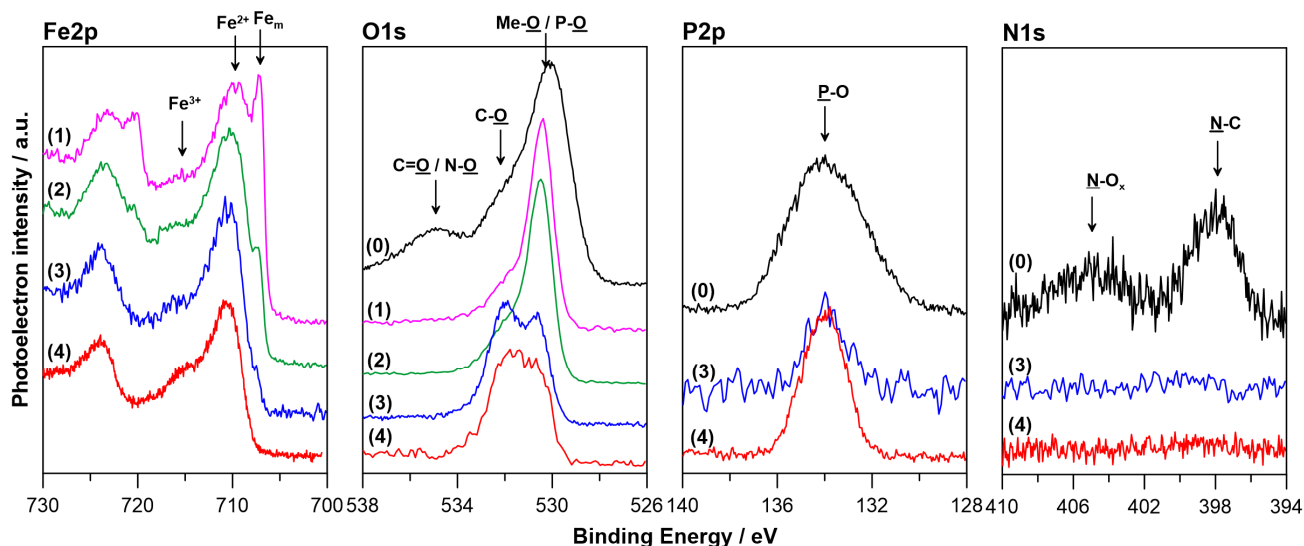

Figure 9. High-resolution XPS analysis for five investigated samples: (0) NPP inhibitor, (1) reference steel sample, (2) corroded steel sample, (3) inhibited steel with C1 of inhibitor, (4) inhibited steel with C2 of inhibitor. Analysis performed in energy range of (from left to right): Fe2p, O1s, P2p and N1s region.

XPS studies were also performed to further confirm the adsorption of NPP and gain more insight about the chemistry of the protective layer formed by the corrosion inhibitor. Fig. 9 depicts high-resolution XPS analysis carried out in the energy range of Fe2p, O1s, P2p and N1s regions for both concentrations of applied corrosion inhibitor, corroded steel sample without addition of the inhibitor, polished steel sample and tested NPP inhibitor itself, for reference purposes. Each investigated sample has been analyzed after 50s of ion beam etching to represent the investigated sample as closely as possible. Its goal was to remove the carbon and oxygen contamination present due to exposure of sample to atmospheric air. Longer etching was unfeasible, as it would lead to complete removal of investigated protective layer. Carbon was excluded from the analysis due to strong overlapping of C-C, C-O, C-N and C-P peaks [82], offering no conclusive information. Its total share in the signal ranged between 11 and 27 at.%.

Analysis carried out in the binding energy range of P2p unequivocally proved the formation of the protective layer on inhibited steel samples, regardless of the concentration of the inhibitor. The signal composes of a single peak doublet, with P2p3/2 energy of 133.2 ± 0.2 eV, which is most typical for phosphate groups [83]. There is no observable energy shift of this peak between investigated inhibitor and inhibited steel samples, suggesting that the chemistry of phosphate bonds has not changed. On the other hand, measurement carried out for NPP in N1s energy range revealed two sub-peaks, typically observable for nitrophenyl [84]. Those were N-C at 398.1 ± 0.1 eV for N-C bonds and 405.0 ± 0.1 eV for N-O bonds. However, no trace of nitrogen was found in signal corresponding to inhibited steel samples.

For iron, three components were included in deconvolution of XPS spectra. Those were metallic iron (707.3 eV), and iron oxides of different oxidation states: Fe^{II} at 710.1 ± 0.1 eV and Fe^{III} at 713.6 ± 0.1 eV [85]. The sub-peak for Fe_m was only observable for reference and corroded steel samples. Its absence in inhibited samples means the higher thickness of the oxide layer. The last analyzed element was oxygen, in the energy range of O1s peak. The exact quantitative analysis might be tricky, due to the fact that peaks for oxygen in phosphates and iron oxides overlap at around 530.3 ± 0.3 eV. Two remaining peaks were used for deconvolution of O1s region: organic C-O / P=O bonds (BE ~531.8 eV) originating from investigated inhibitor and exposure to atmospheric air as well as organic C=O / N-O bonds (BE of 534.6 eV). The complete quantitative study of investigated samples is presented in Table 5.

Table 5. Percentage contribution (atomic %) of each Fe2p, P2p, O1s and N1s peak for investigated samples: (0) NPP inhibitor, (1) reference steel sample, (2) corroded steel sample, (3) inhibited steel with C1 of inhibitor, (4) inhibited steel with C2 of inhibitor.

	Fe_m	Fe^{II}	Fe^{III}	P-O	O-Me/ O-P	O-C/ O=P	O=C*	N-Ox	N-C
(0)	--	--	--	24.0	36.1	24.1	10.4	1.9	3.5
(1)	9.3	30.7	17.9	--	28.8	13.3	--	--	--
(2)	2.8	26.3	18.2	--	34.9	17.8	--	--	--
(3)	--	18.2	14.4	9.1	21.4	36.9	--	--	--
(4)	--	7.5	6.0	21.8	31.2	33.5	--	--	--

XPS analysis provides proof that protective properties of NPP originate from formation of the passive layer on the surface of investigated steel sample. This layer is composed of a mixture of phosphates and iron oxides. Even low concentration **C1** of NPP is sufficient to produce the layer, however the increase of NPP concentration consequences in a greater share of phosphates. Me-O/P-O ratio is 1.52 for **C1** and only 0.43 for **C2** concentration. The higher the concentration of NPP the lower the contribution of O-C bonds, which might originate from exposition of corrosion products to atmospheric air. Nitrophenyl, which is a part of the inhibitor compound does is not involved in formation of the protective passive layer.

p-Nitrophenyl phosphate disodium salt undergoes hydrolysis in aqueous electrolytes according to the reaction:
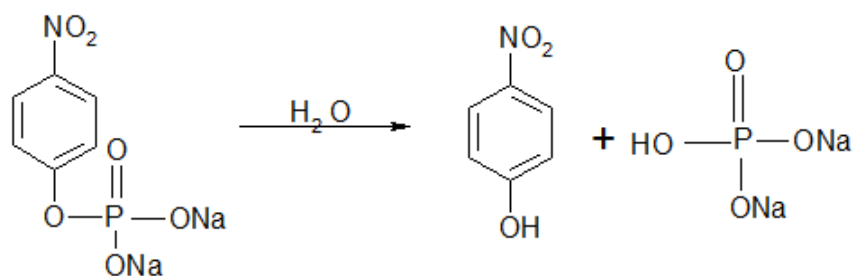
XPS surface analysis proves that the corrosion products on the surface of investigated steel consist of iron oxides and some phosphorous compounds. Presence of nitric groups or aromatic rings was not detected, corroborating with hydrolysis theory. Literature reports suggest that the presence of Fe^{2+} and Fe^{3+}, produced as a result of steel corrosion, can additionally act as catalyst of NPP hydrolysis reaction [85-88].

Corrosion inhibition of NPP should be considered as synergistic action between hydrolysis products: p-nitrophenolate and disodium hydrogen phosphate. Similar to inorganic nitrides, p-nitrophenolate acts as anodic inhibitor, a direct passivator. Presence of nitric groups inhibits the anodic dissolution of iron through the formation of iron oxides, such as magnetite ($FeO*Fe_2O_3$) and maghemit (γ-Fe_2O_3), at electrode surface [89-91]. Simultaneously, nitric groups are reduced to amines during a sequence of elimination, addition and substitution reactions involving H^+ ions and electrons produced during anodic dissolution of metal [92-95]. Inhibition effect is synergistically enhanced by the presence of disodium hydrogen phosphates, acting as an indirect passivator [96]. Here, metal protection mechanism involves covering its surface with thin adsorption films, which requires presence of atmospheric oxygen or other oxidants. As a result, the corrosion process is inhibited by formation of the protective layer on steel surface. This layer is composed of hydrated iron oxides, additionally sealed by iron phosphates effectively blocking anodic active sites.

3.2.3. PAS studies

The lifetime components τ_1 and τ_2, and their intensities I_1 and I_2 of the as-polished, corroded, and inhibited CSA516 samples are shown in Fig. 10.
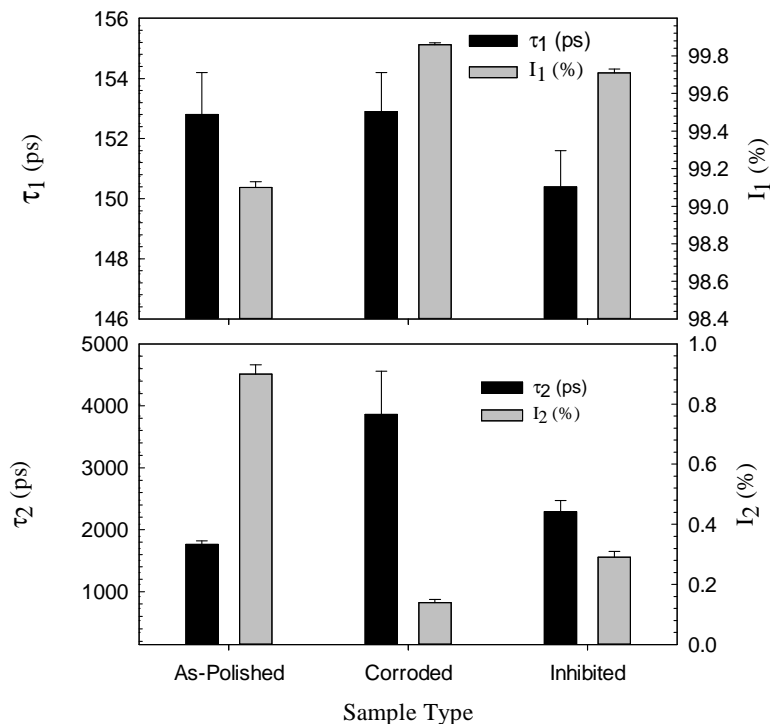
Figure 10. The lifetime components τ_1 and τ_2 and their intensities I_1 and I_2 recorded for the as-polished, corroded and inhibited CSA516 samples. Corroded and inhibited samples were obtained after 24 h of immersion in NaCl solutions without (corroded) and with 0.01 M NPP (inhibited) at 25 °C.

The results indicate that the lifetime component τ_1 dominates with intensity >99% in all CSA516 samples. The values of τ_1 are in a good agreement with those calculated for vacancy-solute complexes for steel components [52]. The τ_1 values of the as-polished and corroded CSA516 samples are almost the same, most probably due to the horizontal attack of the aggressive anions in solution and subsequent formation of shallow pits, revisit Fig. 7a. This shallow attack of the corrosion process makes the bulk composition of both samples identical. We are therefore not surprising why the τ_1 values of both samples are consistent, see Fig. 10, as a consequence of the bulk examination nature of the positron radioactive source-based PAS. The decrease of the τ_1 value for the inhibited sample may be due to the electron abundance of the adsorbed phosphate group, as evidenced from XPS examinations (Fig. 9). On the other hand, the I_1 values of the corroded and inhibited samples are somewhat larger than that of the as-polished sample, Fig. 10. For the corroded sample, this can be explained by the increase of vacancy defect caused by the corrosion process. The value of I_1 for the inhibited sample is expected to be close to that of the as-polished one. However, the result was not so and it is found to be somewhat larger. There should be some vacancies (defects) in the inhibitor film itself behind the unexpected increase in the value of I_1.
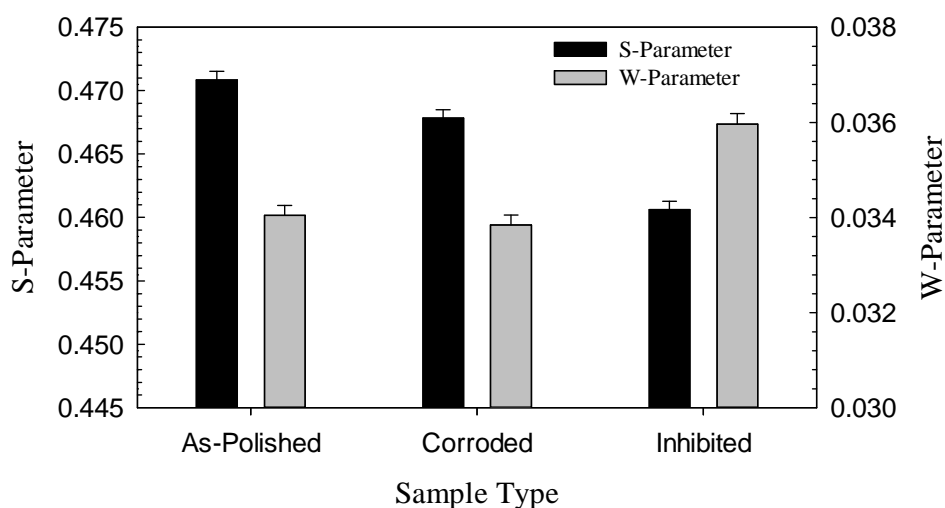
Figure 11. The *S*- and *W*- parameters recorded for the as-polished, corroded and inhibited CSA516 samples. The corroded and inhibited samples were prepared as shown in the caption of Figure 10.

The *o*-Ps lifetime component τ_2 with very small fraction of I_2 ranged from 0.14 to 0.9% was observed for CSA516 samples. The average radius of the microcracks caused by the vacancies clustering of as-polished, corroded and NPP inhibited samples are found to be 0.27±0.01, 0.42±0.08 and 0.31±0.02 nm, respectively. The mean volumes of these microcracks, considered to be spherical in shape, are 0.08, 0.31 and 0.12 nm^3 for the as-polished, corroded and inhibited CSA516 samples, respectively. The results indicate that the concentration of microcracks (I_2) of the corroded sample is the lowest among the others (as-polished and inhibited) due to the coalesce interfering. Such interfering of the microcracks can be clearly observed on the morphology of the corroded sample, Fig. 7(a). The observed increase of τ_2 value of the corroded sample compared with those of the as-polished and inhibited ones, and consequently the size increase of the microcracks, supports the vacancy agglomeration process. Further inspection of Fig. 10 reveals that the value of I_2 recorded for the inhibited sample is about one-third lower than that measured for the as-polished one, as the adsorbed phosphate groups blocked most of the microcracks.

The calculated *S*– and *W*–parameters of the CSA516 samples are shown in Fig. 11. The results show that the *S*- and W-parameters are almost the same, within the experimental errors, for the as-polished and corroded samples. This result can be explained on the basis of the following reasons: (i) the low concentration of the microcracks (I_2 <1%), (ii) the shallow attack of the corrosion process (Fig. 7a) that only destroyed very thin layer of the as-polished sample, and finally (iii) the bulk examination nature of the used PADB technique. The inhibited sample recorded the lowest value for the *S*-parameter among the others due to the decrease of microcracks concentration caused by the blocking effect of the adsorbed phosphate groups. On the contrary, the highest value of the *W*-parameter was measured for the inhibited sample because of the increase of the high momentum core electrons of the adsorbed phosphate groups. Figure 12 depicts the relation between the *S*- and *W*-parameters. There is

no linear relation between the *S*- and *W*-parameters, which indicates that the defects in studied samples have different structure.
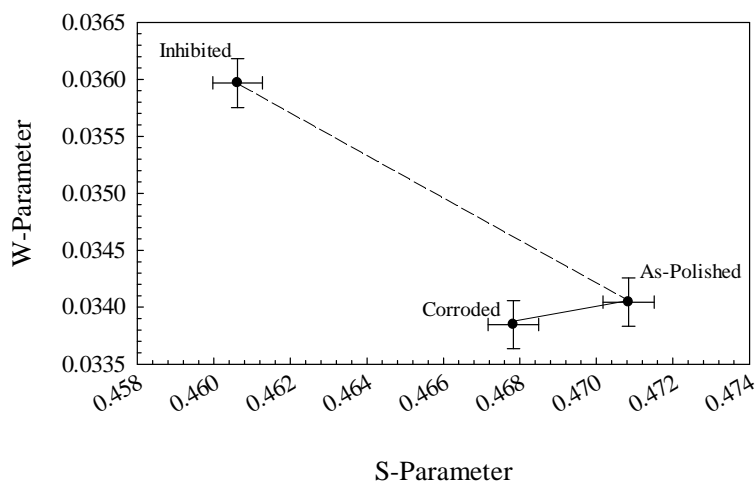

Figure 12. The relation between the *S*- and *W*- parameters measured for the as-polished, corroded and inhibited CSA516 samples.

It is worth mentioning that the defect structure of the as-polished and corroded samples are almost the same due to the shallow attack of corrosion. However, the inhibited sample exhibited different defect structure. Perhaps the adsorbed layer of the inhibitor itself has its own defects.

4. CONCLUSION

The authors have proved beyond a reasonable doubt that NPP offers good inhibitor efficiency (up to 97% for the highest concentration of 0.02 M NPP) and that it serves as anodic inhibitor, suppressing the anodic part of the corrosion reaction. XPS surface analysis proved the absence of nitrogen compounds on the surface of investigated electrodes. Authors claim that the p-nitrophenolate, which is one of NPP hydrolysis products, directly forms iron oxide layer, analogous to the one found on the electrode surface, while the nitric groups are reduced and does not take part in formation of the layer. On the other hand, the phosphorous compounds originate from disodium hydrogen phosphates, second product of NPP hydrolysis. Here, XPS corroborates with FT-IR study. The PAL and PADB techniques are used to study the microstructure and defect structure changes of the as-polished, corroded and inhibited carbon steel samples. The parameters of the PAS techniques confirmed the shallow-type corrosion process of CSA516 in NaCl solutions, and the inhibition performance of the tested compound.

References

1. M.F. Montemor, *Surf. Coat. Technol.*, 258 (2014) 17.
2. P.P. Deshpande, N.G. Jadhav, V.J. Gelling, D. Sazou, *J. Coat. Technol. Res.*, 11 (2014) 473.
3. Norsok Standard: Cathodic Protection (M-503). Edition 3, May 2007.
4. M. Finšgar, J. Jackson, *Corros. Sci.,* 86 (2014) 17.
5. B. Elsener: "Mixed-in Inhibitors", "COST 521: Corrosion of Steel in Reinforced Concrete Structures. Prevention – Monitoring – Maintenance", Final Workshop 18-19 February, Luxembourg, 2002.
6. P. R. Roberge, Handbook of corrosion engineering, New York: Mc GrawHill Hand- book, 1999.
7. R. Naderi, M. Mahdavian, M.M. Attar, *Electrochim. Acta*, 54 (2009) 6892.
8. P.C. Okafor, C.B. Liu, X. Liu, Y.G. Zheng, F. Wang, C.Y. Liu, *J. Solid State Electrochem.*, 14 (2010) 1367.
9. H. Tavakoli, T. Shahrabi,M.G. Hosseini, *Mater. Chem. Phys.*, 109 (2008) 281.
10. M. Hosseini, S.F.L.Mertens, M.R. Arshadi, *Corr. Sci.*, 45 (2003) 1473.
11. R. Fuchs-Godec, M.G. Pavlovic, *Corros. Sci.*, 58 (2012) 192.
12. R. Solmaz, E. Altunbas, A. Doner, G. Kardas, *Corros. Sci.*, 53 (2011) 3231.
13. X. Li, S. Deng, H. Fu, X. Xie, *Corros. Sci.*, 56 (2014) 29.
14. S. Marcelin, N. Pébère, *Corros. Sci.*, 57 (2015) 66.
15. H. Gao, Q. Li , Y. Dai, F. Luo, H.X. Zhang, *Corros. Sci.*, 52 (2010) 1603.
16. V.S. Sastri, Green Corrosion Inhibitors. Theory and Practice. John Wiley & Sons, New York, 1998.
17. R. Martinez-Palou, J. Rivera, L.G. Zepeda, A.N. Rodríguez, M.A. Hernandez, J. Marín-Cruz, A. Estrada, *Corrosion,* 60 (2004) 465.
18. M.A. Arenas, A. Conde, J. de Damborenea, *Corros. Sci.*, 44 (2002) 511.
19. G. Moretti, F. Guidi, G. Grion, *Corros. Sci.* 46 (2004) 387.
20. W.A. Badawy, K.M. Ismail, A.M. Fathi, *Electrochim. Acta*, 51 (2006) 4182.
21. K.M. Ismail, *Electrochim. Acta*, 52 (2007) 7811.
22. B.E.A. Rani, B.B.J. Basu, *Int. J. Corros.*, 2012 (2012) 1.
23. M.R.E. Aly, H. Shokry, T. Sharshar, M.A. Amin, J. *Molecular Liquids*, 214 (2016) 319.
24. M.A. Amin, O.A. Hazzazi, F. Kandemirli, M. Saracoglu, *Corrosion*, 68 (2012) 688.
25. M.A. Amin, M.M. Ibrahim, *Corros. Sci.*, 53 (2011) 873.
26. M.A. Amin, *Corros. Sci.*, 52 (2010) 3243.
27. M.A. Amin, S.S. Abd El Rehim, A.S. El-Lithy, *Corros. Sci.*, 52 (2010) 3099.
28. M.A. Amin, K.F. Khaled, Q. Mohsen, H.A. Arida, *Corros. Sci.*, 52 (2010) 1684.
29. M.A. Amin, *Chinese Chem. Letts.*, 21 (2010) 341.
30. M.A. Amin, S.S.Abd El Rehim, M.M. El-Naggar, H.T.M. Abdel-Fatah, *J. Mat. Sci.*, 44 (2009) 6258.
31. M.A. Amin, S.S. Abd El Rehim, H.T.M. Abdel-Fatah, *Corros. Sci.*, 51 (2009) 882.
32. M.A. Amin, H.H. Hassan, O.A. Hazzazi, M.M. Qhatani, *J. Appl. Electrochem.*, 38 (2008) 1589.
33. C. MacKintosh, C. Protein Phosphorylation: A Practical Approach. 221. New York,1993.
34. S. Zhuo, J.C. Clemens, D.J. Hakes, D. Barford, J.E. Dixon, *J. Biol. Chem.*, 268 (1993) 17754.
35. A. Takai, G. Mieskes, *Biochem. J.,* 275 (1991) 233.
36. J. Wang, F. You, J. Yin, G. Gao, *J. Mater. Sci. Technol.*, 17 (2001) 482.
37. Y.C. Jean, P.E. Mallon, D.M. Schrader, Principles and applications of positron &positronium chemistry: World Scientific Publishing Co. Pte. Ltd., New Jersey, 2003.
38. V. Krsjak, V. Grafutin, O. Ilyukhina, R. Burcl, A. Ballesteros, P. Hähner, *J. Nucl. Mater.*, 421 (2012) 97.

39. R. Pietrzak, W. Smiatek, R. Szatanik, *Acta Phys. Polon. A*, 110 (2006) 667.
40. R. Zaleski, M. Gorgol, K. Zaleski, *Phys. Procedia*, 35 (2012) 92.
41. V. Kršjak, *J. Electrical Engineering*, 60 (2009) 198.
42. E.E. Abdel-Hady, *Nucl. Instr. and Meth. B*, 221 (2004) 225.
43. A. Dupasquier, A.P. Mills Jr., Positron Spectroscopy of Solids, IOS Press, Amsterdam, 1995
44. X. Wu, P. Asoka-Kumar, K.G. Lynn, K.R. Hebert, *J. Electrochem. Soc.*, 141 (1994) 3361.
45. H. Wu, K.R. Hebert, T. Gessmann, K.G. Lynn, *J. Electrochem. Soc.*, 149 (2002) B108.
46. K.R. Hebert, T. Gessmann, K.G. Lynn, P. Asoka-Kumar, *J. Electrochem. Soc.*, 151 (2004) B22.
47. Y.C. Wu, P.H. Li, X.D. Xue, S.J. Wang, A.Kallis, P.G. Coleman, T. Zhai, *J. Physics*, 262 (2011) 012065.
48. J.Š. Veterníková, J. Degmová, V. Slugeň, Applied Physics of Condensed Matter: Proceedings of the 20th International Conference, 2014, pp. 166–169.
49. ASTM G1-03 "Standard Practice for Preparing, Cleaning, and Evaluating Corrosion Test", 2011.
50. T. Sharshar, M.L. Hussein, *Nucl. Instr. Meth. A*, 546 (2005) 584.
51. J. Kansy, *Nucl. Instr. Meth. A*, 374 (1996) 235.
52. J. Kuriplach, O. Melikhova, C. Domain, C.S. Becquart, D. Kulikov, L. Malerba, M. Hou, A. Almazouzi, C.A. Duque, A.L. Morales, *Appl. Surf. Sci.*, 252 (2006) 3303.
53. M. Eldrup, D. Lightbody, J.N. Sherwood, *Chem. Phys.*, 63 (1981) 51.
54. K. Ito, Y. Ujihira, T. Yamashita, K. Horie, *J. Polym. Sci. B*, 37 (1999) 2634.
55. I.K. Mackenzie, J.A. Eady, R.R. Gingerich, *Phys. Lett. A*, 33 (1970) 279.
56. M.A. Abdel-Rahman, M. Abdel-Rahman, M. Abo-Elsoud, M.F. Eissa, Y.A. Lotfy, E.A. Badawi, *Prog. Phys.*, 3 (2006) 66.
57. J. Dryzek, E. Dryzek, *Tribol. Lett.*, 17 (2004) 147.
58. B.A. Lindsley, A.R. Marder, *Wear*, 225 (1999) 510.
59. M.A. Amin, Q. Mohsen, N.Y. Mostafa, N. El-Bagoury, A. Al-Refaie, A.K. Bairamov, S. Al-Maaesab, E.M. Murillo, S.A. Al-Qahtani, *Int. J. Electrochem. Sci.,* 9 (2014) 2631.
60. O.K. Abiola, J.O.E. Otaigbe, *Corros. Sci.*, 51 (2009) 2790.
61. E.M. Sherif, R.M. Erasmus, J.D. Comins, *Corros. Sci.*, 50 (2008) 3439.
62. M. Abdallah, M.M. El-Naggar, *Mat. Chem. Phys.*, 71 (2001) 291.
63. M. Abdallah, H.E. Megahed, M. A. Radwan, E. Abdfattah, *J. Am. Sci.*, 8 (2012) 49.
64. M. Abdallah, I. Zaafrany, A. Fawzy, M.A. Radwan, E. Abdfattah, *J. Am. Sci.*, 9 (2013) 580.
65. O.A. Hazazi, M. Abdallah, *Int. J. Electrochem. Sci.*, 8 (2013) 8138.
66. U. Schulz, M. Peters, Fr.-W Bach, G. Tegeder, *Mat. Sci. Eng. A*, 362 (2003) 61.
67. M.A. Amin, S.S. Abd EI-Rehim, E.E.F. El-Sherbini, O.A. Hazzazi, M.N. Abbas, *Corros. Sci.*, 51 (2009) 658.
68. M.A. Amin, K.F. Khaled, *Corros. Sci.*, 52 (2010) 1194.
69. M.A. Amin, K.F. Khaled, S.A. Fadl-Allah, *Corros. Sci.*, 52 (2010) 140.
70. S. Hong, W. Chen, Y. Zhang, H.Q. Luo, M. Li, N.B. Li, *Corros. Sci.*, 66 (2013) 308
71. N.O. Obi-Egbedi a, I.B. Obot, *Corros. Sci.*, 53 (2011) 263.
72. ASTM G31-72 "Standard Practice for Laboratory Immersion Corrosion Testing of Metals" (1999).
73. H.J. Flitt, D.P. Schweinsberg, *Corros. Sci.*, 47 (2005) 2125.
74. H.J. Flitt, D.P.Schweinsberg, *Corros. Sci.*, 47 (2005) 3034.
75. B. Rosborg, J. Pan, C. Leygraf, *Corros. Sci.*, 47 (2005) 3267.
76. E. McCafferty, *Corros. Sci.*, 47 (2005) 3202.
77. ASTM, Standard Practice for Calculation of Corrosion Rates and Related Information From Electrochemical Measurements (G 102-89 (Reapproved)) 1994.
78. M. Stern, A.L. Geary, *J. Electrochem. Soc.*, 104 (1957) 56.

79. X. Gao, X. Wu, Z. Zhang, *J. Supercritical Fluids*, 42 (2007) 157.
80. L. Tan, K. Sridharan, T. R. Allen, *J. Nuclear Mater.*, 348 (2006) 263.
81. K. Nakamoto, Infrared and Raman Spectra of Inorganic and Coordination Compounds, Part B, Applications in Coordination, Organometallic, and Bioinorganic Chemistry, 6th Edition, 2009.
82. R. Bogdanowicz, M. Sawczak, P. Niedzialkowski, P. Zieba, B. Finke, J. Ryl, J. Karczewski, T. Ossowski, *J. Phys. Chem. C*, 118 (2014) 8014.
83. E.O. Lopez, A. Mello, M. Farina, A.M. Rossi, A.L. Rossi, *Surf. Coat. Technol.*, 279 (2015) 16.
84. S.S.C. Yu, E.S.Q. Tan, R.T. Jane, A.J. Downard, *Langmuir*, 23 (2007) 11074.
85. Z. Petrovic, M. Metikos-Hukovic, R. Peter, M. Petravic, *Int. J. Electrochem. Sci.*, 7 (2012) 9232.
86. N.P. Sadler, Ch.Ch. Chuang, R.M. Milburn, *Inorg. Chem.*, 34 (1995) 402.
87. J.R. Morrow, W.C. Trogler, *Inorg. Chem.*, 27 (1998) 3387.
88. J. Rawlings, A.C. Hengge, W.W. Cleland, *J. Am. Chem. Soc.*, 119 (1997) 542.
89. J.D. Kim, S.I. Pyun, *Corros. Sci.*, 38 (1996) 1093.
90. M.S. Odziemkowski, T.T. Schuhmacher, R.W. Gillham, E.J. Reardon, *Corros. Sci.*, 40 (1998) 371.
91. J.H. Fan, H.W. Wang, D.L. Wu, Z.G. Liu, L.M. Ma, *J. Chem. Technol. Biotechnol.*, 86 (2011) 1295.
92. B. Jafarpour, P.T. Imhoff, P.C. Chiu, *J. Contam. Hydrol.*, 76 (2005) 87.
93. H.C.B. Hansen, G. Susanne, E. Marianne, *Appl. Clay. Sci.*, 18 (2001) 81.
94. W.Y. Xu, T.Y. Gao, J.H. Fan, *J. Hazard. Mater.*, 123 (2005) 232.
95. J.H. Fan, H.W. Wang, *Environ. Sci.Pollut. Res.*, 22 (2015) 9932.
96. S.A.M. Refaey, S.S. Abd El-Rehim, F. Taha, M.B. Saleh, R.A. Ahmed, *Appl. Surf. Sci.*, 158 (2000) 190.